

# Leveraging Spatio-Temporal Dependency for Skeleton-Based Action Recognition

Jungho Lee<sup>1</sup> Minhyeok Lee<sup>1</sup> Suhwan Cho<sup>1</sup> Sungmin Woo<sup>1</sup> Sangyoun Lee<sup>1</sup>

<sup>1</sup>Yonsei University

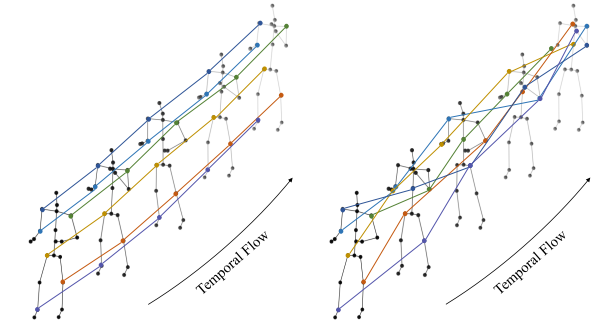
{2015142131, hydragon516, chosuhwan, smw3250, syleee}@yonsei.ac.kr

## Abstract

Skeleton-based action recognition has attracted considerable attention due to its compact skeletal structure of the human body. Many recent methods have achieved remarkable performance using graph convolutional networks (GCNs) and convolutional neural networks (CNNs), which extract spatial and temporal features, respectively. Although spatial and temporal dependencies in the human skeleton have been explored, spatio-temporal dependency is rarely considered. In this paper, we propose the Inter-Frame Curve Network (IFC-Net) to effectively leverage the spatio-temporal dependency of the human skeleton. Our proposed network consists of two novel elements: 1) The Inter-Frame Curve (IFC) module; and 2) Dilated Graph Convolution (D-GC). The IFC module increases the spatio-temporal receptive field by identifying meaningful node connections between every adjacent frame and generating spatio-temporal curves based on the identified node connections. The D-GC allows the network to have a large spatial receptive field, which specifically focuses on the spatial domain. The kernels of D-GC are computed from the given adjacency matrices of the graph and reflect large receptive field in a way similar to the dilated CNNs. Our IFC-Net combines these two modules and achieves state-of-the-art performance on three skeleton-based action recognition benchmarks: NTU-RGB+D 60, NTU-RGB+D 120, and Northwestern-UCLA.

## 1. Introduction

Action recognition is one of the most important video understanding tasks used in various applications such as virtual reality and human-computer interaction. Recent studies on action recognition are divided into two methods, RGB-based [29, 31] and skeleton-based methods [2, 4, 23, 24, 34]. Action recognition using the skeleton modality receives a video sequence with the three-dimensional coordinates of major human joints as its input. Skeleton-based action recognition has the advantage of being able to create a lightweight model with low computational complexity by compactly compressing the structure of the human body. In addition, it has the advantage of robustness in that it is not affected by background noise, weather, and lighting conditions unlike RGB-based methods.



(a) Spatio-Temporal GCN

(b) Inter-Frame Curve Network

Figure 1. Comparison of temporal flows of spatio-temporal GCN (a) and IFC module of our model (b). (b)'s curves make the model's spatio-temporal receptive field larger by aggregating different nodes for different frames, whereas (a) treats the temporal features of each node independently.

Earlier approaches [7, 8, 13, 20, 36] extract features by dealing with every joint independently, which means that they do not consider information between structurally correlated human joints. However, the connections between human joints are identified as a graph structure after Yan *et al.* [34] has proposed spatio-temporal graph convolutional networks (GCNs) for the skeleton modality. Recent approaches [2, 4, 6, 24] adopt the GCNs as their baseline and attempt to enlarge the receptive field on the spatial domain.

However, methods based on Yan *et al.*'s GCNs have several limitations. (1) Because their spatial and temporal modules exist independently, spatio-temporal correlations of major human joints as its input. Skeleton-based action recognition has the advantage of being able to create a lightweight model with low computational complexity by compactly compressing the structure of the human body. In addition, it has the advantage of robustness in that it is not affected by background noise, weather, and lighting conditions unlike RGB-based methods.

However, methods based on Yan *et al.*'s GCNs have several limitations. (1) Because their spatial and temporal modules exist independently, spatio-temporal correlations

tions cannot be leveraged directly. In other words, the spatio-temporal dependency of skeletal video data is rarely reflected to the model because existing temporal modules extract features without taking account of direct spatio-temporal correlations. (2) Because they use graphs that include only the connectivity of physically adjacent joints, their networks with such graphs have small spatial receptive fields. Although several methods [2, 24] for constructing graphs with a large receptive field using self-attention mechanism have been proposed, they still use the physically adjacent graph structure. Their graphs are less effective because the graphs with the self-attention mechanism have much smaller element values than physically adjacent graphs. In addition, Liu *et al.* [18] propose a multi-scale graph that identifies the relationship between structurally distant nodes, but there is still a limitation that the model complexity is too high. Although it is possible to enlarge the receptive field using deeper networks, this causes high computational complexity, and it is still challenging to directly identify the connections to the structurally distant nodes.

To solve limitation (1), we propose an Inter-Frame Curve (IFC) module to reflect direct spatio-temporal dependencies in a skeleton sequence. In addition to applying temporal convolution to aggregate node-wise sequential features, we construct curves that consider global sequential features for every node and apply them to the input feature map. To create the curves, we choose the most highly correlated nodes between all adjacent frames and connect them for large spatio-temporal receptive field. Fig. 1 compares the temporal flows of the spatio-temporal GCN for existing methods [2, 24, 34] and our proposed method. Fig. 1 (a) shows that the model reflects only features of the same nodes in every frame, while Fig. 1 (b) shows that the model considers the spatio-temporal correlations through the curves that take account of features of different nodes in adjacent frames. Inspired by [32], we use an aggregation module to effectively combine all the curves and apply them to the input feature map.

To handle limitation (2), we propose a Dilated Graph Convolution (D-GC) to apply the widely used dilated kernels to GCNs and to have large spatial receptive field for skeletal modality. GCNs for the human skeleton aggregate inward-facing (centripetal), identity, and outward-facing (centrifugal) features, unlike convolutional neural networks (CNNs), which aggregate left, identity, and right pixels features. To apply the dilated kernel to such GCNs, we create adjacency matrices to identify structurally distant relationships by modifying centripetal and centrifugal matrices. Inspired by [28], we present a spatial module divided into several branch operations to effectively utilize our D-GCs. Those branch operations consider large spatial receptive fields by having various dilation values. Furthermore, our proposed model has low computational complexity be-

cause the spatial module is divided into several branches. Meanwhile, dilated graph convolution has already been introduced by Li *et al.* [14] for 3D point clouds analysis task. However, Li *et al.*'s dilated graph convolution is completely different from what we propose and is not suitable for human skeletal modality. First, this method does not utilize the given adjacency matrices, but instead uses dynamic graph via k-nearest neighborhood (k-NN) algorithm. In addition, because k-NN alone cannot identify all the physically adjacent nodes, the inability to utilize the given adjacency matrices reduces the robustness of the action recognition model. The second reason is that Li *et al.*'s method requires a lot of GPU memory for skeleton sequences. It causes very high GPU memory consumption to construct graphs by computing all pairwise distances between all the nodes for every GCN layer.

To verify the superiority of our IFC-Net, extensive experiments are conducted on three skeleton-based action recognition benchmark datasets: NTU-RGB+D 60 [22], NTU-RGB+D 120 [15], and Northwestern-UCLA [30].

Our main contributions are summarized as follows:

- We propose the inter-frame curve (IFC) module to consider the direct spatio-temporal correlation between different nodes of different frames.
- We propose a dilated graph convolution (D-GC) operation that makes the model have a large spatial receptive field by modifying the given skeletal adjacency matrices into matrices for dilated kernels.
- Our proposed network outperforms existing state-of-the-arts methods on three benchmarks for skeleton-based action recognition.

## 2. Related Work

### 2.1. Skeleton-Based Action Recognition

Previous skeleton-based action recognition methods [7, 13, 21] do not consider the relationships between joint nodes for the human skeleton but treat all the joint nodes independently. However, Yan *et al.* [34] treats this modality as a graph structure. Most recent methods [2, 18, 24, 25] tend to rely on GCNs to deal with spatial correlation. They reflect the subordinate correlations of nodes by identifying the relationships between adjacent joint nodes. In particular, models with graph structures and a self-attention mechanism [2, 23] show remarkable performance. In addition, many RNN-based and CNN-based temporal modules have been proposed to deal with action recognition sequence data defined as time series.

However, there are drawbacks to these methods, and the first is that structurally distant nodes are treated almost independently because of their small spatial receptive fields,

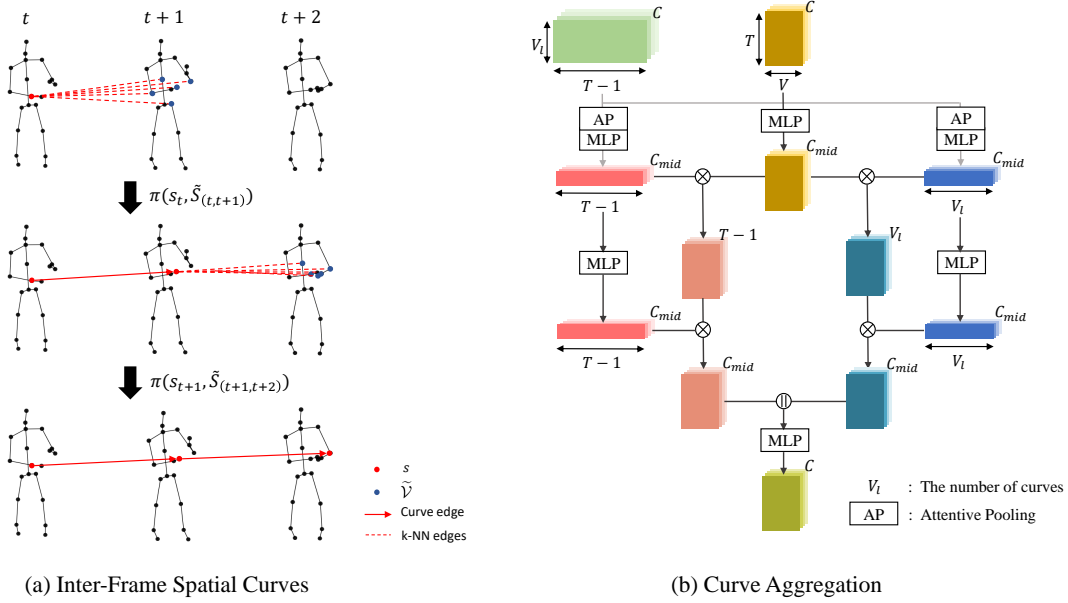


Figure 2. (a) Process of constructing an inter-frame spatial curve and (b) the curve aggregation module that applies the curves to the input feature map  $\mathbf{F}_{in}$ . The dotted line in (a) is the relationship between the query node and the key nodes extracted by the inter-frame k-NN. The node selection policy  $\pi$  adopts the node of the highest correlation score with the query node as the next point in the curve.  $\parallel$  and  $\times$  denote concatenation and matrix multiplication, respectively.

because the given graph considers only the adjacent relationships of nodes. To treat this limitation, learnable graph structures with self-attention mechanisms [2, 6, 24] are proposed. However, these structures use not only the graphs with self-attention mechanisms, but also given graph with adjacent connections. In other words, even if the receptive fields of their models are enlarged with self-attention mechanisms, they do not highlight the appropriate nodes much because they are highly biased to the given graph. Second, although several methods for handling skeleton sequences [16, 17] have been proposed, most of them do not take account of spatio-temporal dependencies because they consider only node-wise sequences. In other words, most recent methods are vulnerable to this dependency because of their low spatio-temporal receptive fields.

## 2.2. Curves for 3D Point Clouds

3D point clouds are unstructured representations of 3D coordinates, tasks for them are to analyze the information for 3D points that exist without any adjacency matrices given. In order to effectively analyze these point clouds, Xiang *et al.* [32] propose CurveNet, which identifies the relationships between every 3D points by aggregating both local and non-local features. In one scene, CurveNet initializes  $n$  starting points and constructs  $n$  curves with length  $l$  by finding the most correlated points. Applying the curves to the feature space, both the local and non-local point con-

nections are identified. We propose an inter-frame spatial curve module that makes the curves applicable to skeletal video data, and effectively increases the spatio-temporal receptive field.

## 3. Methodology

### 3.1. Inter-Frame Curve Module

In this subsection, we describe the inter-frame curve (IFC) module to consider the direct spatio-temporal correlations of skeleton sequences.

**Inter-Frame Curve Generation.** In order to construct a curve between frame  $t$  and  $(t+1)$ , it is essential to find and connect the key node  $\tilde{v}_{t+1}$  that is most semantically close to the query node  $v_t$ , where  $v_t$  is a specific node on frame  $t$ . To specify the node  $\tilde{v}_{t+1}$ , we select  $k$  nodes in frame  $(t+1)$  that are physically close to the query node. The nodes are selected through inter-frame k-NN, which applies Euclidean distance-based k-NN algorithms between all adjacent frames to obtain the physically closest  $k$  nodes. If the query node  $v_t$  and obtained key node  $\tilde{v}_{t+1}$  refer to structurally identical locations, the model may identify only the same nodes between adjacent frames. Therefore, it hinders a model to have a large spatio-temporal receptive field. To prevent this problem, we apply the k-NN algorithm while excluding the node of frame  $(t+1)$  that is located in the

same structural position as query node  $v_t$ . The proposed inter-frame k-NN is as follows:

$$\tilde{\mathcal{V}}_{(t,t+1)} = \sum_{v \in V} \text{k-NN}(v_t, \mathcal{V}_{t+1} - \{v_{t+1}\}), \quad (1)$$

where  $\tilde{\mathcal{V}}_{(t,t+1)}$  denotes a set of  $k$  nodes in frame  $(t+1)$  that are the physically closest nodes to the query node  $v_t$ , and  $(\mathcal{V}_{t+1} - \{v_{t+1}\})$  refers to the node set in frame  $(t+1)$  except the node that is structurally the same as  $v_t$ .

To construct effective curves, the key node most highly correlated with the query node  $v_t$  should be extracted using the node set  $\tilde{\mathcal{V}}_{(t,t+1)}$  created by inter-frame k-NN. For this extraction process, we propose an extended method for the node selection policy  $\pi$  in [32] to choose the key node  $\tilde{v}_{t+1}$ . The policy in [32] reflects only nodes in a single frame without considering the temporal feature space. To consider the time domain as well, we apply a new node selection policy  $\pi$  to choose the key node by reflecting the key node features and physically adjacent node set  $\tilde{\mathcal{V}}_{(t,t+1)}$ .

$$s_{t+1} = \pi \left( s_t, \tilde{\mathcal{S}}_{(t,t+1)} \right), \quad 1 \leq t \in \mathbb{Z}^+ \leq T-1, \quad (2)$$

where  $s_t$  and  $s_{t+1}$  refer to the embedded spaces of the query and the key nodes,  $\tilde{\mathcal{S}}_{(t,t+1)}$  denotes the embedded features of  $\tilde{\mathcal{V}}_{(t,t+1)}$ , and  $T$  is the length of the skeleton sequence, which is equal to  $(\text{curve length} + 1)$ . We build a learnable policy  $\pi$  to consider the features of query node  $v_t$  and the features of extracted node set  $\tilde{\mathcal{V}}_{(t,t+1)}$  by aggregating them. We obtain a new agent feature map  $\mathbf{M}_{\text{agent}}$  by passing those features through an agent MLP layer. Then, we extract the node with the highest correlation score in adjacent frame  $(t+1)$  via  $\mathbf{M}_{\text{agent}}$ . Extracted key node  $\tilde{v}_{t+1}$  refers to next embedded space  $s_{t+1}$ , and we concatenate the extracted node to the end node of the previous curve. The process to choose the key node is as follows:

$$\mathbf{M}_{\text{agent}} = \text{MLP} \left( s_t \parallel \tilde{\mathcal{S}}_{(t,t+1)} \right), \quad (3)$$

$$\pi \left( s_t, \tilde{\mathcal{S}}_{(t,t+1)} \right) = \mathbf{F}_{\text{in}} \left[ \arg \max(\mathbf{M}_{\text{agent}}) \right], \quad (4)$$

where  $\parallel$  denotes the concatenation operation and  $\mathbf{F}_{\text{in}}$  refers to the input feature map.

However, the weights of  $\mathbf{M}_{\text{agent}}$  are not updated smoothly during backpropagation due to the undifferentiable  $\arg \max$  function. To solve this problem, we use a Gumbel Softmax function [11, 35], which is computed as a one-hot vector for forward operation, and updates the weight using the results of the softmax function for backward propagation. With these methods, our curves are represented as follows:

$$\text{curve} = [s_1 \rightarrow s_2 \rightarrow \dots \rightarrow s_T] \in \mathbb{R}^{C \times (T-1)}. \quad (5)$$

Because we set all joint nodes in the first frame to be the starting points of the curves, the shape of the integrated curve is  $\text{curves} \in \mathbb{R}^{C \times (T-1) \times V}$ , where  $V$  denotes the number of joint nodes.

**Curve Aggregation.** Inspired by [32], we use an aggregation module to effectively apply the curves to the input feature map. The process of the curve aggregation module is shown in Fig. 2 (b). By applying the curve aggregation, the model can consider both the relationship between every curves (inter-curve features  $\mathbf{F}_{\text{inter}}$ ) and the relationship between nodes existing in one curve (intra-curve features  $\mathbf{F}_{\text{intra}}$ ). For computational efficiency, we concatenate two extracted features  $\mathbf{F}_{\text{inter}}$  and  $\mathbf{F}_{\text{intra}}$ , using a bottleneck structure.  $\mathbf{F}_{\text{inter}}$  is computed as follows:

$$\tilde{\mathbf{F}}_{\text{inter}} = \text{softmax}(\mathbf{F}_{\text{in}} \times \text{curve}_{\text{inter}}), \quad (6)$$

$$\mathbf{F}_{\text{inter}} = \text{MLP}_{\text{inter}}(\text{curve}_{\text{inter}}) \times \tilde{\mathbf{F}}_{\text{inter}}, \quad (7)$$

where  $\text{curve}_{\text{inter}}$  is the curve feature map after attentive pooling [10], and  $\text{MLP}_{\text{inter}}$  is a layer that transforms the curve features. The  $\text{curve}_{\text{inter}}$  is applied to the input feature map  $\mathbf{F}_{\text{in}}$  while the existing feature map shape  $\in \mathbb{R}^{C \times T \times V}$  is preserved. The  $\mathbf{F}_{\text{intra}}$  is obtained in a way similar to Eq. (6) and Eq. (7). Our curve aggregation module is shown in Fig. 2 (b). To aggregate the two different features, we use the following method:

$$\mathbf{F}_{\text{out}} = (\mathbf{F}_{\text{inter}} \parallel \mathbf{F}_{\text{intra}}) \mathbf{W}_{\text{agg}} \in \mathbb{R}^{C \times T \times V}, \quad (8)$$

where  $\mathbf{W}_{\text{agg}} \in \mathbb{R}^{2C \times C}$  integrates  $\mathbf{F}_{\text{inter}}$  and  $\mathbf{F}_{\text{intra}}$ . Finally, a new feature map  $\mathbf{F}_{\text{out}}$  is generated, where the curve features are applied to the input feature map  $\mathbf{F}_{\text{in}}$ , and it enables the model to consider spatio-temporal dependencies.

### 3.2. Dilated Graph Convolution

There have been many attempts [2, 18, 24] to increase the spatial receptive field of GCNs, but it still remains a challenging problem. To solve this problem, we propose dilated convolution for the graph structure in this subsection.

**Kernel Analogy from CNNs to GCNs.** The kernels for CNNs are applied to networks to aggregate local features in pixel units. In particular, for convolution to a single axis, local features are largely divided into [“Left”, “Identity”, “Right”] when the size of the kernel is 3. Those features are integrated into a representative information that identifies adjacent pixels by weighted summation. For example, if the “Left”, “Identity”, and “Right” features are symbolized as -1, 0, and 1, respectively, a kernel with a dilation of 2 can be expressed as [-2, 0, 2]. Therefore, the CNN operation with a dilation of  $d$  is as follows:

$$\mathbf{F}_{\text{out}} = \sum_{k \in [-1, 0, 1]} \mathbf{F}_{\text{in}}[p + k * d] \mathbf{W}_k, \quad (9)$$

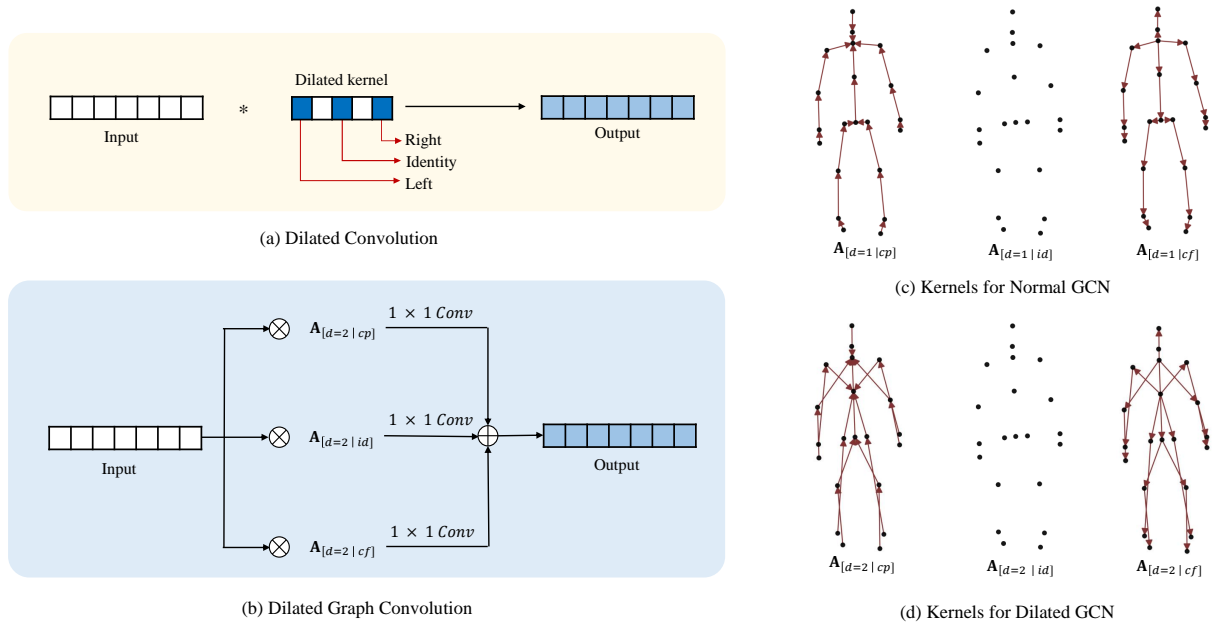


Figure 3. Comparison with structures of dilated convolution (a) and dilated graph convolution (b), and comparison of normal graph kernels (c), which are the given adjacency matrices and dilated graph kernels (d). The arrows in (c) and (d) include information about the direction of the edges and the start and end points. The dilation value for all kernels is fixed to 2.

where  $p$  denotes location of the pixel and  $\mathbf{W}_k$  denotes the weights of the kernel-wise MLP layer.

In non-Euclidean geometry, the concept of “Right” and “Left” for CNNs cannot be used because those directions cannot be defined, especially for graph structures. Yan *et al.* [34] first propose a method for selecting the root node and dividing the kernel into [“Centripetal” ( $cp$ ), “Identity” ( $id$ ), and “Centrifugal” ( $cf$ )] to aggregate the local features for skeleton-based action recognition. According to this policy, because the kernels in non-Euclidean geometry are represented as adjacent matrices, the dilated GCN operation is as follows:

$$\Phi(\mathbf{F}_{in}, d) = \sum_{k \in [cp, id, cf]} \mathbf{A}_{[d|k]} \mathbf{F}_{in} \mathbf{W}_k, \quad (10)$$

where  $\mathbf{A}_{[d|k]}$  denotes a normalized adjacency matrix according to the dilation given the direction of the kernel, and  $\Phi$  refers to the D-GC operation. For example, GCNs with a dilation of 2 aggregate node features by skipping one adjacent node. Our D-GC operation is systematically similar to that of the CNN (e.g., number of parameters, floating point operations) and a comparison of two modules is shown in Fig. 3 (a) and (b). In addition, because the  $id$  kernel itself denotes an identity matrix,  $\mathbf{A}_{[d|id]}$  is the same matrix as  $\mathbf{A}_{[d=1|id]}$ . In other words, adjacency matrices for a kernel size of 3 and a dilation of 2 are divided into  $[\mathbf{A}_{[d|cp]}, \mathbf{A}_{[d|id]}, \mathbf{A}_{[d|cf]}]$ . The kernels for GCNs with adjacent connectivity and D-GCs are shown in Fig. 3 (c) and (d).

**Dilated Graph Convolution.** To construct adjacency matrices with the dilated kernels, we borrow Liu *et al.* [18]’s method. The  $k$  power of an adjacency matrix includes edges that are structurally  $k$  steps away from the query node. However, if only the power of the adjacency matrix is used to consider nodes that are  $k$  steps away, the output matrix includes the paths back to the query node. To exclude these paths, we use the difference between the  $d$  power and the  $(d - 1)$  power of the adjacency matrix:

$$\tilde{\mathbf{A}}_{[d|k]} = \lambda \left( (\tilde{\mathbf{A}}_{[d=1|k]} + \mathbf{I})^d \right) - \lambda \left( (\tilde{\mathbf{A}}_{[d=1|k]} + \mathbf{I})^{d-1} \right), \quad (11)$$

$$\mathbf{A}_{[d|k]} = \mathbf{D}_{[d|k]}^{-\frac{1}{2}} \tilde{\mathbf{A}}_{[d|k]} \mathbf{D}_{[d|k]}^{-\frac{1}{2}}, \quad (12)$$

where  $\tilde{\mathbf{A}}$  and  $\mathbf{A}$  stand for the unnormalized and normalized adjacency matrices, respectively, and  $\mathbf{D}$  denotes the degree matrix for normalization.  $\lambda$  function receives input as matrix and replaces all the elements greater than 1 with 1 and all values less than 1 with 0. Without  $\lambda$  function, it hinders the optimization and convergence of the model since the elements for the overlapping paths become largely biased values.  $\lambda$  function allows the model to converge stably while avoiding those biases on the edges for overlapping paths.

### 3.3. Network Architecture

**Overall Architecture.** We adopt the architecture of [34] as our baseline, which includes 10 spatio-temporal blocks.



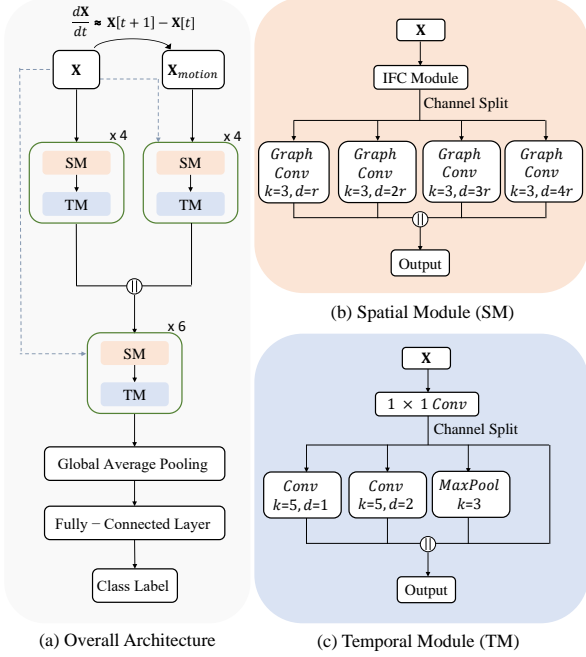


Figure 4. Overall architecture of the model (a) and the spatial (b) and temporal modules (c). Graph convolutions of the spatial module and convolutions of the temporal module are the operations for the node axis and the frame axis, respectively. In addition, the dotted lines in (a) denote the input fed to all spatio-temporal blocks for inter-frame k-NN based on physical distance.

The output channels of each block are 64, 64, 64, 64, 128, 128, 128, 256, 256, and 256, and each block includes independent spatial and temporal module, and residual connections [9] for stable learning. For data composed of the time-series  $x_t$ ,  $y_t$ , and  $z_t$  coordinates, we utilize the motion vector  $\frac{d\mathbf{X}}{dt} \approx [x_{t+1} - x_t, y_{t+1} - y_t, z_{t+1} - z_t]$  differently from existing methods [2, 4, 25]. Coordinate and motion data pass through four spatio-temporal blocks independently, and then they are concatenated to take account of those two modalities in a single network. Our overall architecture is shown in Fig. 4 (a).

**Spatial Module.** Inspired by [1, 7], we construct a multi-branch spatial module based on D-GC. Our spatial module has 2 layers in series and 4 operations in parallel, as shown in Fig. 4 (b). This module first passes the input feature map  $\mathbf{F}_{in}$  through a feature transformation block, which is the IFC module. For efficient computational complexity, we place the IFC modules only on specific layers of the model, and place point-wise convolution on the remaining layers. After the block, we divide the transformed features into four, and feed them into four branch operations with an extension

factor  $r$ , similar to [1], where the kernel size is fixed to 3:

$$\mathbf{F}_{out} = \bigparallel_{\tilde{d} \in [1, 2, 3, 4]} \Phi(\mathbf{F}_{in}, d = r * \tilde{d}), \quad (13)$$

where  $\Phi$  denotes the D-GC operation in Eq. (10) and  $d$  denotes the dilation of each GCN operation. Then, all four branch operation results are concatenated to create a new output feature map  $\mathbf{F}_{out}$ .

**Temporal Module.** We adopt the multi-scale temporal convolution of [2] as the temporal module shown in Fig. 4 (c). This module includes one feature transformation block and four branch operations, similar to the spatial module. Two of their operations are temporal convolutions with dilations of 1 and 2, which have a kernel size of 5. The remaining operations are a temporal convolution with a kernel size of 3 and dilation of 1, and a max pooling layer with a kernel size of 3. After all four operations are completed, the output feature map is constructed by concatenating all the resulting feature maps.

## 4. Experiments

### 4.1. Datasets

**NTU-RGB+D 60.** NTU-RGB+D 60 [22] is a large skeleton-based action recognition dataset that contains 56,880 action sequences. All the sequences are performed by 40 subjects and are classified into a total of 60 classes. This dataset is captured by three Microsoft Kinect v2 cameras, each of which captures at horizontal angles of  $45^\circ$ ,  $0^\circ$ , and  $-45^\circ$ . At least one and at most two subjects exist in an action sample. We follow two benchmarks suggested by the authors of the dataset. (1) Cross-Subject (X-Sub): The actions of 20 out of 40 subjects are used for training, and the actions of the remaining 20 are used for validation. (2) Cross-View (X-View): Two of the three camera views are used for training, and the other one is used for validation.

**NTU-RGB+D 120.** NTU-RGB+D 120 [15] is a dataset in which 57,367 action sequences are added from the NTU-RGB+D 60 dataset. All action sequences are performed by 106 objects, and are classified into a total of 120 classes. All the samples are captured with three camera views. In addition, the dataset is captured under 32 settings including different locations and backgrounds. We use two benchmarks proposed by the authors of this dataset. (1) Cross-Subject (X-Sub): The actions of 53 objects out of 106 objects are used for training, and the rest are used for validation. (2) Cross-Setup (X-Set): Among 32 numbered settings, even-numbered settings are used for training, and odd-numbered settings are used for validation.

Methods	Year	# Ensemble Models	NTU-RGB+D 60		NTU-RGB+D 120	
			X-Sub (%)	X-View (%)	X-Sub (%)	X-Set (%)
ST-GCN [34]	AAAI 2018	-	81.5	88.3	82.5	84.2
2s-AGCN [24]	CVPR 2019	2	88.5	95.1	88.5	95.1
DGNN [23]	CVPR 2019	2	89.9	96.1	-	-
AGC-LSTM [26]	CVPR 2019	2	89.2	95.0	-	-
Shift-GCN [5]	CVPR 2020	4	90.7	96.5	85.9	87.6
DC-GCN+ADG [4]	ECCV 2020	4	90.8	96.6	86.5	88.1
MS-G3D [18]	CVPR 2020	2	91.5	96.2	86.9	88.4
MST-GCN [3]	AAAI 2021	4	91.5	96.6	87.5	88.8
Skeletal GNN [37]	ICCV 2021	4	91.6	96.7	87.5	89.2
CTR-GCN [2]	ICCV 2021	4	92.4	96.8	88.9	90.6
Ta-CNN+ [33]	AAAI 2022	2	90.7	95.1	85.7	87.3
EfficientGCN-B4 [27]	TPAMI 2022	4	91.7	95.7	88.3	89.1
STF [12]	AAAI 2022	2	92.5	96.9	88.9	89.9
InfoGCN [6]	CVPR 2022	4	92.7	96.9	89.4	90.7
Ours		2	92.5	96.7	89.3	90.7
Ours		4	<b>93.0</b>	<b>97.1</b>	<b>89.9</b>	<b>91.3</b>

Table 1. Comparison of the top-1 accuracy (%) with the state-of-the-arts on NTU-RGB+D 60, 120 datasets. For a fair comparison, the number of ensemble streams is fixed to 2 or 4.

**Northwestern-UCLA.** Northwestern-UCLA [30] is an action recognition dataset containing 1494 skeleton sequences. All the action samples are classified into 10 classes that are captured by three cameras at different angles. We use the protocol proposed by the authors: two of the three camera views are used for training and the other is for validation.

## 4.2. Experimental Settings

In our experiments, we set the number of epochs to 90, and we apply a warm-up strategy [9] to the first five epochs for more stable learning. We adopt an SGD optimizer with a Nesterov momentum of 0.9 and a weight decay of 0.0004. The initial learning rate is set to 0.1, and we reduce the learning rate to 0.0001 through the cosine annealing scheduler [19]. We use Zhang *et al.* [38]’s data preprocessing method for NTU-RGB+D 60 and 120 datasets, and we set the batch size to 64. For the Northwestern-UCLA dataset, we use the data preprocessing method by Cheng *et al.* [5] and set the batch size to 16. In addition, the IFC module is applied to the 3-rd, 6-th, and 9-th blocks of the 10 spatio-temporal blocks for memory efficiency, and pointwise convolution is applied to the remaining blocks. Our experiments are conducted on a single RTX 3090 GPU.

## 4.3. Comparison with the State-of-the-Arts

Many recent state-of-the-art models [2, 4, 25] use the ensemble method by training four data streams, i.e., joint, bone, joint motion, and bone motion. However, as networks with only the joint (bone) motion stream show inferior performances than networks with joint (bone) stream, learning two streams independently is inefficient. Unlike them,

Methods	# Ensemble Models	Northwestern-UCLA Top-1 (%)
SGN [38]	-	92.5
AGC-LSTM [26]	2	93.3
Shift-GCN [5]	4	94.6
DC-GCN+ADG [4]	4	95.3
CTR-GCN [2]	4	96.5
InfoGCN [6]	4	96.6
Ours	4	<b>97.4</b>

Table 2. Comparison of the top-1 accuracy (%) with the state-of-the-arts on Northwestern-UCLA dataset.

we train joint and joint motion streams on one network, as shown in Fig. 4 (a). We also train bone and bone motion streams on the network. We adopt the ensemble method of models trained with the extension factor  $r$  as 1 and 2 without considering the motion stream separately, where  $r$  is explained in Sec. 3.3. In other words, we use the models with the joint ( $r = 1$ ), bone ( $r = 1$ ), joint ( $r = 2$ ), and bone ( $r = 2$ ) streams for our ensemble method.

We evaluate performance on three skeleton-based action recognition benchmarks. The performance comparisons for the NTU-RGB+D 60 [22] and 120 [15] datasets and the Northwestern-UCLA [30] datasets are shown in Tab. 1 and Tab. 2. We set the number of ensemble streams to 2 or 4 for a fair comparison, and our IFC-Net outperforms state-of-the-arts on all datasets. For the NTU-RGB+D 120 dataset, even with 2 ensembles, IFC-Net shows comparable performance ( $-0.1\%$  and  $+0.0\%$ ) when compared with [6], a state-of-the-art model with four ensembles.

Methods	motion	$k$	Curve Aggregation	X-Sub (%)	X-Set (%)
Baseline	✓	-	-	85.1	86.6
IFC-Net	✓	5	✗	85.7	87.4
IFC-Net	✓	6	✗	85.8	87.3
IFC-Net	✓	7	✗	85.7	87.3
IFC-Net	✓	5	✓	86.0	<b>87.9</b>
IFC-Net	✓	6	✓	<b>86.2</b>	<b>87.9</b>
IFC-Net	✓	7	✓	86.0	87.7

Table 3. Comparison of performance with different IFC modules according to  $k$  of inter-frame k-NN and the presence of the curve aggregation module.

Methods	branches	Extension Ratio $r$	# Param.	X-Sub (%)	X-Set (%)
Baseline	-	-	1.33 M	85.1	86.6
IFC-Net	1	-	1.85 M	85.8	87.2
IFC-Net	2	1	1.46 M	85.6	87.3
IFC-Net	2	2	1.46 M	85.6	87.5
IFC-Net	2	3	1.46 M	85.8	87.6
IFC-Net	4	1	1.30 M	<b>86.2</b>	87.8
IFC-Net	4	2	1.30 M	85.9	<b>87.9</b>
IFC-Net	4	3	1.30 M	85.9	<b>87.9</b>

Table 4. Comparison of complexity and classification performance according to the number of branches and expansion ratio  $r$  of the spatial module.

#### 4.4. Ablation Study

In this section, we conduct several experiments to prove the superiority of our proposed modules. The performance described in this section refers to cross-subject and cross-setup accuracy on the NTU-RGB+D 120 joint stream.

**Inter-Frame Curve Module.** In order to prove the effectiveness of the IFC module, we specify a baseline model in which the temporal module of [2] is applied to the architecture in [34]. According to Tab. 3, the performances increases by 1.1% and 1.3% than baseline performances. We conduct experiments by dividing  $k$  by 5, 6, and 7 to determine how many neighboring nodes are extracted via inter-frame k-NN. Without the curve aggregation module, the models with a  $k$  value of 5 and 6 show the highest performance, and with the curve aggregation module, the model with a  $k$  value of 6 shows the highest performance. Overall, the models with IFC modules show better performance with a larger margin than the baseline. In addition, the IFC modules introduce a negligible extra model complexity of 0.07 M more parameters to the baseline model, regardless of the value of  $k$ . Visualizations for the generated curves are shown in our Appendix.

**Dilated Graph Convolution.** To verify the superiority of our D-GC, we conduct experiments by setting the number

	X-Sub (%)	X-Set (%)	GFLOPs	# Param.
DC-GCN [4]	84.0*	86.1*	1.83	3.37 M
MS-G3D [18]	84.9*	86.8*	5.22	3.22 M
MST-GCN [3]	84.6*	86.7*	3.58	2.92 M
CTR-GCN [2]	84.9	86.5*	1.97	1.46 M
InfoGCN [6]	85.1	86.3	1.84	1.57 M
IFC-Net				
w/o motion	85.2	87.0	<b>1.51</b>	<b>1.20 M</b>
w/ motion	<b>86.2</b>	<b>87.9</b>	1.73	1.30 M

Table 5. Comparison of computational and model complexity of the state-of-the-arts. \* denotes that we experiment based on the released code.

of branches of the spatial module to 1, 2, and 4, and the extension ratio  $r$  to 1, 2, and 3. Tab. 4 shows that performance of our model does not change according to extension ratio  $r$ . However, considering that there is a large performance margin between the ensemble results with two models and four models, as shown in Tab. 1, this heuristically shows that the learning pattern of the model is also different if the extension ratio is different. In addition, the larger the number of branches, the lower the model complexity, and the better the performance as the receptive field increases. In particular, the model with 4 branch layers shows the best performance regardless of the value of  $r$ .

#### 4.5. Computational Complexity

A comparison of the efficiency between our model and other state-of-the-arts is shown in Tab. 5. Our IFC-Net without motion data has fewer parameters (-0.37 M) than [2] and shows lower computational complexity (-0.33 GFLOPS) than [4]. Our model shows slightly better performances than the state-of-the-arts without motion data. Moreover, our model with motion data shows the best performance with a large margin of all the models, and it has fewer parameters (-0.27 M) than [2] and lower computational complexity (-0.10 GFLOPS) [4].

### 5. Conclusions

In this paper, we propose a novel inter-frame curve network (IFC-Net) for skeleton-based action recognition, which consists of a spatial module with an inter-frame curve (IFC) module and multi-branch dilated graph convolution (D-GC). Our IFC module constructs spatio-temporal curves by connecting the most highly correlated nodes in successive frames, which significantly increases the spatio-temporal receptive field. Our D-GC is carefully designed for skeleton-based action recognition to give the model a large spatial receptive field through dilated graph kernels. By combining these two methods, we implement IFC-Net and demonstrate its superiority through extensive experiments, and our proposed model outperforms existing methods on three benchmarks.



## Appendix

### A. Complexity of Ensemble Models

In our main paper, we compare the complexity of our model to that of the state-of-the-art models by a single stream. Further, we compare the performance and complexity of those models, as shown in Tab. 6. Our model has the lowest model and computational complexity and shows the best performance. Although the performance of our model is slightly better than 6-ensemble InfoGCN [6] model, our model has about 1.81 times less parameters and 1.60 times lower FLOPs than InfoGCN because it requires six models for ensemble while our model needs four. Even compared to 4-ensemble InfoGCN, our model has 1.21 times less parameters and 1.06 times lower FLOPs and outperforms InfoGCN by a large margin. It verifies the superiority and efficiency of our proposed model.

### B. Additional Experimental Results

Every experimental result of NTU-RGB+D 60, 120 and Northwestern-UCLA datasets are shown in Tab. 7 and Tab. 8. By applying our ensemble method, every single model with different extension ratio  $r$ s and streams contribute to achieving the best performance.

### C. Qualitative Results of Inter-Frame Curves

We propose Inter-Frame Curve (IFC) module to identify spatio-temporal dependencies of the human skeleton. To verify the superiority of our proposed module qualitatively, we attach the trained curves of several data samples as shown in Fig. 5. For the “Brush teeth”, “Drink water”, “Check time”, and “Salute” classes, their curves start from every node in the first frame, and those curves tend to proceed toward hand or arm nodes. Inspired by human visual recognition, it is reasonable that the hand gestures should be highlighted for those classes. Similarly, the curves of “Put on the shoe”, “Kicking”, and “Kicking something” classes tend to directed toward lower body. It is also reasonable that the leg gestures are important for those classes.

Methods	# Ensembles	NTU-RGB+D 120		Multi-Stream	
		X-Sub (%)	X-Set (%)	# Params.	FLOPs
DC-GCN [4]	4	86.5	88.1	13.48 M	7.32 G
MS-G3D [18]	2	86.9	88.4	6.44 M	10.44 G
MST-GCN [3]	4	87.5	88.8	11.68 M	14.32 G
CTR-GCN [2]	4	88.9	90.6	5.84 M	7.88 G
InfoGCN [6]	4	89.4	90.7	6.28 M	7.36 G
InfoGCN [6]	6	89.8	91.2	9.42 M	11.04 G
IFC-Net	4	<b>89.9</b>	<b>91.3</b>	<b>5.20 M</b>	<b>6.92 G</b>

Table 6. Comparison of computational and model complexity of the state-of-the-art ensemble models.

Stream	Extension ratio $r$	NTU-RGB+D 60		NTU-RGB+D 120	
		X-Sub (%)	X-View (%)	X-Sub (%)	X-Set (%)
Joint	1	91.0	95.8	86.1	87.8
	2	90.9	95.8	85.8	87.9
Bone	1	91.1	95.3	87.1	88.7
	2	91.2	95.3	87.3	88.6
Ensemble		<b>93.0</b>	<b>97.1</b>	<b>89.9</b>	<b>91.3</b>

Table 7. Experimental results of NTU-RGB+D 60 and 120 datasets according to data streams and extension ratio  $r$  of our spatial module.

Stream	Extension ratio $r$	Northwestern-UCLA Top-1 (%)
Joint	1	93.5
	2	95.9
Bone	1	94.0
	2	93.8
Ensemble		<b>97.4</b>

Table 8. Experimental results of Northwestern-UCLA dataset according to data streams and extension ratio  $r$  of our spatial module.

## References

- [1] Liang-Chieh Chen, George Papandreou, Iasonas Kokkinos, Kevin Murphy, and Alan L Yuille. Deeplab: Semantic image segmentation with deep convolutional nets, atrous convolution, and fully connected crfs. *IEEE transactions on pattern analysis and machine intelligence*, 40(4):834–848, 2017. 6
- [2] Yuxin Chen, Ziqi Zhang, Chunfeng Yuan, Bing Li, Ying Deng, and Weiming Hu. Channel-wise topology refinement graph convolution for skeleton-based action recognition. In *Proceedings of the IEEE/CVF International Conference on Computer Vision*, pages 13359–13368, 2021. 1, 2, 3, 4, 6, 7, 8, 9
- [3] Zhan Chen, Sicheng Li, Bing Yang, Qinghan Li, and Hong Liu. Multi-scale spatial temporal graph convolutional network for skeleton-based action recognition. In *Proceedings of the AAAI Conference on Artificial Intelligence*, volume 35, pages 1113–1122, 2021. 7, 8, 9
- [4] Ke Cheng, Yifan Zhang, Congqi Cao, Lei Shi, Jian Cheng, and Hanqing Lu. Decoupling gcnn with dropgraph module for skeleton-based action recognition. In *Proceedings of the European Conference on Computer Vision (ECCV)*, 2020. 1, 6, 7, 8, 9
- [5] Ke Cheng, Yifan Zhang, Xiangyu He, Weihang Chen, Jian Cheng, and Hanqing Lu. Skeleton-based action recognition with shift graph convolutional network. In *Proceedings of the IEEE/CVF Conference on Computer Vision and Pattern Recognition*, pages 183–192, 2020. 7
- [6] Hyung-gun Chi, Myoung Hoon Ha, Seunggeun Chi, Sang Wan Lee, Qixing Huang, and Karthik Ramani. Infogcn: Representation learning for human skeleton-based action recognition. In *Proceedings of the IEEE/CVF Conference on Computer Vision and Pattern Recognition*, pages 20186–20196, 2022. 1, 3, 7, 8, 9

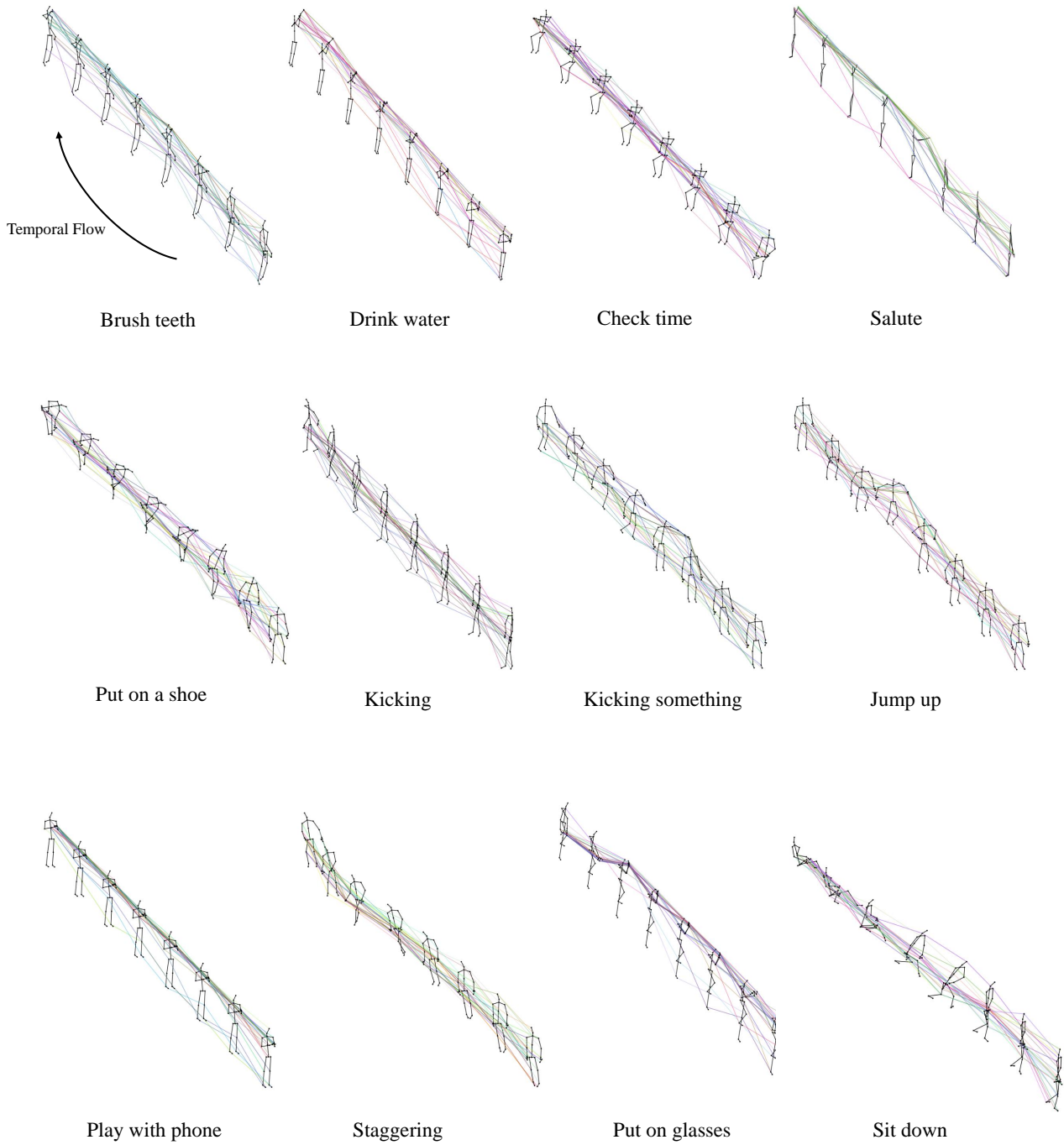


Figure 5. Visualization of trained curves for several data samples.

- [7] David K Duvenaud, Dougal Maclaurin, Jorge Iparraguirre, Rafael Bombarell, Timothy Hirzel, Alán Aspuru-Guzik, and Ryan P Adams. Convolutional networks on graphs for learning molecular fingerprints. *Advances in neural information processing systems*, 28, 2015. [1](#), [2](#), [6](#)
- [8] Will Hamilton, Zhitao Ying, and Jure Leskovec. Inductive representation learning on large graphs. *Advances in neural information processing systems*, 30, 2017. [1](#)
- [9] Kaiming He, Xiangyu Zhang, Shaoqing Ren, and Jian Sun. Deep residual learning for image recognition. In *Proceed-*

- ings of the *IEEE Conference on Computer Vision and Pattern Recognition*, pages 770–778, 2016. 6, 7
- [10] Qingyong Hu, Bo Yang, Linhai Xie, Stefano Rosa, Yulan Guo, Zhihua Wang, Niki Trigoni, and Andrew Markham. Learning semantic segmentation of large-scale point clouds with random sampling. *IEEE Transactions on Pattern Analysis and Machine Intelligence*, 2021. 4
- [11] Eric Jang, Shixiang Gu, and Ben Poole. Categorical reparameterization with gumbel-softmax. *arXiv preprint arXiv:1611.01144*, 2016. 4
- [12] Lipeng Ke, Kuan-Chuan Peng, and Siwei Lyu. Towards to-at spatio-temporal focus for skeleton-based action recognition. *arXiv preprint arXiv:2202.02314*, 2022. 7
- [13] Thomas Kipf, Ethan Fetaya, Kuan-Chieh Wang, Max Welling, and Richard Zemel. Neural relational inference for interacting systems. In *International Conference on Machine Learning*, pages 2688–2697. PMLR, 2018. 1, 2
- [14] Guohao Li, Matthias Müller, Ali Thabet, and Bernard Ghanem. Deepgcns: Can gcns go as deep as cnns? In *The IEEE International Conference on Computer Vision (ICCV)*, 2019. 2
- [15] Jun Liu, Amir Shahroudy, Mauricio Perez, Gang Wang, Ling-Yu Duan, and Alex C Kot. Ntu rgb+ d 120: A large-scale benchmark for 3d human activity understanding. *IEEE Transactions on Pattern Analysis and Machine Intelligence*, 42(10):2684–2701, 2019. 2, 6, 7
- [16] Jun Liu, Amir Shahroudy, Dong Xu, Alex C Kot, and Gang Wang. Skeleton-based action recognition using spatio-temporal lstm network with trust gates. *IEEE transactions on pattern analysis and machine intelligence*, 40(12):3007–3021, 2017. 3
- [17] Jun Liu, Gang Wang, Ping Hu, Ling-Yu Duan, and Alex C Kot. Global context-aware attention lstm networks for 3d action recognition. In *Proceedings of the IEEE conference on computer vision and pattern recognition*, pages 1647–1656, 2017. 3
- [18] Ziyu Liu, Hongwen Zhang, Zhenghao Chen, Zhiyong Wang, and Wanli Ouyang. Disentangling and unifying graph convolutions for skeleton-based action recognition. In *Proceedings of the IEEE/CVF Conference on Computer Vision and Pattern Recognition*, pages 143–152, 2020. 2, 4, 5, 7, 8, 9
- [19] Ilya Loshchilov and Frank Hutter. Sgdr: Stochastic gradient descent with warm restarts. *arXiv preprint arXiv:1608.03983*, 2016. 7
- [20] Federico Monti, Davide Boscaini, Jonathan Masci, Emanuele Rodola, Jan Svoboda, and Michael M Bronstein. Geometric deep learning on graphs and manifolds using mixture model cnns. In *Proceedings of the IEEE conference on computer vision and pattern recognition*, pages 5115–5124, 2017. 1
- [21] Mathias Niepert, Mohamed Ahmed, and Konstantin Kutikov. Learning convolutional neural networks for graphs. In *International conference on machine learning*, pages 2014–2023. PMLR, 2016. 2
- [22] Amir Shahroudy, Jun Liu, Tian-Tsong Ng, and Gang Wang. Ntu rgb+ d: A large scale dataset for 3d human activity analysis. In *Proceedings of the IEEE Conference on Computer Vision and Pattern Recognition*, pages 1010–1019, 2016. 2, 6, 7
- [23] Lei Shi, Yifan Zhang, Jian Cheng, and Hanqing Lu. Skeleton-based action recognition with directed graph neural networks. In *Proceedings of the IEEE/CVF Conference on Computer Vision and Pattern Recognition*, pages 7912–7921, 2019. 1, 2, 7
- [24] Lei Shi, Yifan Zhang, Jian Cheng, and Hanqing Lu. Two-stream adaptive graph convolutional networks for skeleton-based action recognition. In *Proceedings of the IEEE/CVF Conference on Computer Vision and Pattern Recognition*, pages 12026–12035, 2019. 1, 2, 3, 4, 7
- [25] Lei Shi, Yifan Zhang, Jian Cheng, and Hanqing Lu. Skeleton-based action recognition with multi-stream adaptive graph convolutional networks. *IEEE Transactions on Image Processing*, 29:9532–9545, 2020. 2, 6, 7
- [26] Chenyang Si, Wentao Chen, Wei Wang, Liang Wang, and Tieniu Tan. An attention enhanced graph convolutional lstm network for skeleton-based action recognition. In *Proceedings of the IEEE/CVF Conference on Computer Vision and Pattern Recognition*, pages 1227–1236, 2019. 7
- [27] Yi-Fan Song, Zhang Zhang, Caifeng Shan, and Liang Wang. Constructing stronger and faster baselines for skeleton-based action recognition. *IEEE Transactions on Pattern Analysis and Machine Intelligence*, 2022. 7
- [28] Christian Szegedy, Wei Liu, Yangqing Jia, Pierre Sermanet, Scott Reed, Dragomir Anguelov, Dumitru Erhan, Vincent Vanhoucke, and Andrew Rabinovich. Going deeper with convolutions. In *Proceedings of the IEEE conference on computer vision and pattern recognition*, pages 1–9, 2015. 2
- [29] Vivek Veeriah, Naifan Zhuang, and Guo-Jun Qi. Differential recurrent neural networks for action recognition. In *Proceedings of the IEEE international conference on computer vision*, pages 4041–4049, 2015. 1
- [30] Jiang Wang, Xiaohan Nie, Yin Xia, Ying Wu, and Song-Chun Zhu. Cross-view action modeling, learning and recognition. In *Proceedings of the IEEE Conference on Computer Vision and Pattern Recognition*, pages 2649–2656, 2014. 2, 7
- [31] Limin Wang, Yuanjun Xiong, Zhe Wang, Yu Qiao, Dahua Lin, Xiaoou Tang, and Luc Van Gool. Temporal segment networks: Towards good practices for deep action recognition. In *European conference on computer vision*, pages 20–36. Springer, 2016. 1
- [32] Tiange Xiang, Chaoyi Zhang, Yang Song, Jianhui Yu, and Weidong Cai. Walk in the cloud: Learning curves for point clouds shape analysis. In *Proceedings of the IEEE/CVF International Conference on Computer Vision (ICCV)*, pages 915–924, October 2021. 2, 3, 4
- [33] Kailin Xu, Fanfan Ye, Qiaoyong Zhong, and Di Xie. Topology-aware convolutional neural network for efficient skeleton-based action recognition. In *Proceedings of the AAAI Conference on Artificial Intelligence*, volume 36, pages 2866–2874, 2022. 7
- [34] Sijie Yan, Yuanjun Xiong, and Dahua Lin. Spatial temporal graph convolutional networks for skeleton-based action

- recognition. In *Thirty-second AAAI Conference on Artificial Intelligence*, 2018. [1](#), [2](#), [5](#), [7](#), [8](#)
- [35] Jiancheng Yang, Qiang Zhang, Bingbing Ni, Linguo Li, Jinxian Liu, Mengdie Zhou, and Qi Tian. Modeling point clouds with self-attention and gumbel subset sampling. In *Proceedings of the IEEE/CVF conference on computer vision and pattern recognition*, pages 3323–3332, 2019. [4](#)
  - [36] Zhitao Ying, Jiaxuan You, Christopher Morris, Xiang Ren, Will Hamilton, and Jure Leskovec. Hierarchical graph representation learning with differentiable pooling. *Advances in neural information processing systems*, 31, 2018. [1](#)
  - [37] Ailing Zeng, Xiao Sun, Lei Yang, Nanxuan Zhao, Minhao Liu, and Qiang Xu. Learning skeletal graph neural networks for hard 3d pose estimation. In *Proceedings of the IEEE/CVF International Conference on Computer Vision*, pages 11436–11445, 2021. [7](#)
  - [38] Pengfei Zhang, Cuiling Lan, Wenjun Zeng, Junliang Xing, Jianru Xue, and Nanning Zheng. Semantics-guided neural networks for efficient skeleton-based human action recognition. In *Proceedings of the IEEE/CVF Conference on Computer Vision and Pattern Recognition*, pages 1112–1121, 2020. [7](#)